

In-plane magnetic field-induced orbital FFLO superconductivity in twisted WSe₂ homobilayers

Jihang Zhu, Yang-Zhi Chou, Yi Huang, and Sankar Das Sarma

Condensed Matter Theory Center and Joint Quantum Institute,

Department of Physics, University of Maryland, College Park, Maryland 20742, USA

We theoretically predict the in-plane magnetic field-induced orbital Fulde-Ferrell-Larkin-Ovchinnikov (FFLO) superconducting states in twisted WSe₂ homobilayers (tWSe₂), focusing on its dependence on layer polarization and Fermi surface geometry. For unpolarized layers, finite-momentum pairing emerges only at low temperatures and above a critical field $B_{c1,\parallel}$. When layer symmetry is broken, finite-momentum pairing is stabilized at any nonzero field, with a critical temperature higher than that of the zero-momentum state. Notably, we identify a phase transition, which separates two distinct FFLO phases, when there are two separate Fermi pockets residing in the two moiré mini-valleys associated with opposite layers. We further discuss the effects of twist angles and applied field directions. Our findings establish tWSe₂ as a promising platform for realizing and manipulating FFLO states via twist angle, displacement field, and filling factor.

Introduction. Recently, robust superconductivity has been observed in twisted WSe₂ homobilayers (tWSe₂) [1, 2], with either small or large layer polarization controlled by a displacement field. Notably, superconducting states emerge near highly resistive [1] or insulating phases [2], prompting various theoretical studies to understand their origin [3–14]. In transition metal dichalcogenides (TMDs), strong Ising spin-orbit coupling (SOC) locks electron spins to the τz direction, where $\tau = \pm 1$ encodes the valley. An in-plane magnetic field B_{\parallel} , albeit much weaker than the Ising SOC effect (~ 500 meV [15] in tWSe₂), shifts the layer-dependent canonical momenta and deforms the Fermi surface (FS) through interlayer coupling. Such B_{\parallel} -induced orbital effects favor finite-momentum Cooper pairing and provide a new pathway for realizing Fulde–Ferrell–Larkin–Ovchinnikov (FFLO) superconductivity [16, 17] purely through orbital effects [18–30].

The FFLO state [16, 17] was originally proposed for s -wave spin-singlet superconductors under a Zeeman field, where spin-split Fermi surfaces (FSs) favor finite-momentum pairing at low temperatures and high magnetic fields exceeding the Pauli paramagnetic limit [32, 33]. While most studies have focused on Zeeman-driven spin mechanisms [34–42], recent work on Ising superconductors has revealed FFLO phenomena arising from both spin and orbital effects [43–47]. The purely orbital FFLO mechanism in tWSe₂ under B_{\parallel} [20] has several distinct features: (i) its two-dimensional (2D) nature mitigates vortex formation, (ii) the system is in the clean limit, with a mean free path much longer than the superconducting coherence length [1], and (iii) the FS is highly tunable via displacement field and doping, allowing rich phenomena driven by layer polarization and FS

geometry [48–54].

In this Letter, we systematically investigate the orbital FFLO superconducting state induced by B_{\parallel} in tWSe₂, as illustrated in Fig. 1(a). We find that the upper critical field $B_{c2,\parallel}$ and the nature of the FFLO phase depend sensitively on layer polarization and FS geometry. For unpolarized layers, finite-momentum pairing emerges only at $T/T_{c0} < \alpha$ (where $\alpha < 1$ and T_{c0} is the zero-field T_c) and above a critical field $B_{c1,\parallel}$. In contrast, when layer symmetry is broken, finite-momentum pairing can be stabilized at any $T/T_{c0} < 1$ and nonzero B_{\parallel} . Remarkably, when two separate Fermi pockets reside in two moiré mini-valleys [region III in Fig. 1(b)], a phase

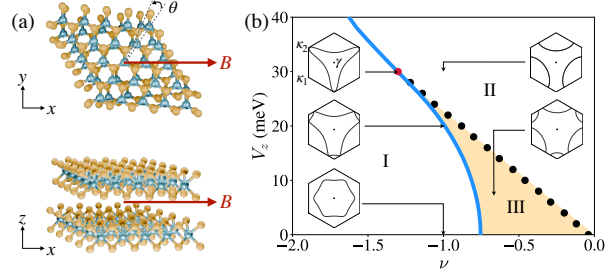


FIG. 1. (a) Top and side views of tWSe₂, with tungsten (blue) and selenium (gold) atoms. (b) Phase diagram of 3.65° tWSe₂ as a function of electron filling factor ν (counting two spin-valley flavors) and displacement field (characterized by the interlayer energy difference V_z), showing different FS geometries. Region I: A single FS at γ . Region II: A single FS at κ_1 ($V_z > 0$). Region III (shaded yellow): Two Fermi pockets at κ_1 and κ_2 , where a phase transition occurs under increasing B_{\parallel} , separating two distinct FF phases, but only when $V_z \neq 0$. The blue line marks the van Hove singularity (VHS). Black dots mark numerically determined boundaries of region III, terminating at a higher-order VHS (red dot) [31].

transition separating two distinct Fulde–Ferrell (FF) phases occurs. Our findings highlight moiré Ising superconductors as a unique platform for realizing and manipulating FFLO states via displacement field, filling factor and twist angle.

Twisted WSe₂ under an in-plane magnetic field. Due to strong Ising SOC, spin-valley locking in tWSe₂ suppresses the Zeeman effect from B_{\parallel} , which we neglect. Under an applied field $\mathbf{B} = B_x \hat{x} + B_y \hat{y}$, the system is described by the Hamiltonian

$$\mathcal{H} = \begin{bmatrix} h_{\mathbf{q}_1+\delta\mathbf{k}_1} + U_1(\mathbf{r}) & T(\mathbf{r}) \\ T^{\dagger}(\mathbf{r}) & h_{\mathbf{q}_2+\delta\mathbf{k}_2} + U_2(\mathbf{r}) \end{bmatrix} + \frac{V_z}{2} \hat{l}_z. \quad (1)$$

Focusing on hole doping, $h_{\mathbf{q}} = -\hbar^2 q^2 / 2m^*$, $\mathbf{q}_l = \mathbf{k} - \boldsymbol{\kappa}_l$ is the momentum relative to the Dirac points $\boldsymbol{\kappa}_l$ of layer $l = 1, 2$. The interlayer energy difference V_z arises from the applied displacement field, and \hat{l}_z is the Pauli matrix acting on the layer degree of freedom. The moiré potentials $U_l(\mathbf{r})$ and interlayer tunneling $T(\mathbf{r})$ take the forms $U_{1,2}(\mathbf{r}) = 2V \sum_{j=1,3,5} \cos(\mathbf{G}_j \cdot \mathbf{r} \mp \psi)$, $T(\mathbf{r}) = w(1 + e^{-i\mathbf{G}_2 \cdot \mathbf{r}} + e^{-i\mathbf{G}_3 \cdot \mathbf{r}})$ [9, 50, 55]. We focus on the twist angle $\theta = 3.65^\circ$ and general properties of orbital FFLO states in this Letter, results of other twist angles can be found in SM [56]. To leading order, $T(\mathbf{r})$ is local and unaffected by B_{\parallel} , which induces a momentum shift $\delta\mathbf{k}_l = e\mathbf{A}_l/\hbar$ in layer l [57–59] via the Peierls phase. In the Landau gauge, $\mathbf{A}_l = B_y z_l \hat{x} - B_x z_l \hat{y}$. Since the two layers are separated along the out-of-plane (z) direction, the momentum shifts satisfy

$$\delta\mathbf{k}_1 - \delta\mathbf{k}_2 = q_B (\sin \theta_B \hat{x} - \cos \theta_B \hat{y}), \quad (2)$$

where θ_B is the angle of \mathbf{B} relative to the x -axis, and $q_B = edB/\hbar = d/l_B^2$, with magnetic length $l_B = \sqrt{\hbar/eB}$ and layer separation $d = 0.7$ in tWSe₂. Due to gauge freedom, in our calculations we choose

$$\begin{aligned} \delta\mathbf{k}_1 &= \frac{q_B}{2} \left[(1 - \bar{l}_z) \sin \theta_B \hat{x} - (1 - \bar{l}_z) \cos \theta_B \hat{y} \right], \quad (3) \\ \delta\mathbf{k}_2 &= \frac{q_B}{2} \left[-(1 + \bar{l}_z) \sin \theta_B \hat{x} + (1 + \bar{l}_z) \cos \theta_B \hat{y} \right]. \end{aligned}$$

$\bar{l}_z \in [-1, 1]$ is the average layer polarization, defined as $\bar{l}_z = \sum_{n\mathbf{k}} \langle n\mathbf{k} | \hat{l}_z | n\mathbf{k} \rangle f_{n\mathbf{k}} / \sum_{n\mathbf{k}} f_{n\mathbf{k}}$ for electron doping and $\bar{l}_z = \sum_{n\mathbf{k}} \langle n\mathbf{k} | \hat{l}_z | n\mathbf{k} \rangle (1 - f_{n\mathbf{k}}) / \sum_{n\mathbf{k}} (1 - f_{n\mathbf{k}})$ for hole doping. By choosing Eq. (3), we ensure that B_{\parallel} does not influence the superconducting state through orbital effects when carriers are fully layer-polarized.

Finite-momentum pairing. We focus on the intervalley intralayer phenomenological BCS pairing interaction within the continuum model framework [9]. Specifically, we assume that B_{\parallel} does not change the

coupling constant of the pairing interaction. Other cases will be discussed at the end of this Letter.

We consider an intervalley intralayer pairing with local attraction [9]. The interacting Hamiltonian for a Cooper pair with momentum \mathbf{q} is

$$\begin{aligned} \mathcal{H}_{\text{int}} = -\frac{g}{A} \sum_{l,\mathbf{k},\mathbf{k}'} \psi_{+,\mathbf{G},l}^{\dagger}(\mathbf{k} + \frac{\mathbf{q}}{2}) \psi_{-,-\mathbf{G},l}^{\dagger}(-\mathbf{k} + \frac{\mathbf{q}}{2}) \\ \psi_{-,-\mathbf{G}',l}(-\mathbf{k}' + \frac{\mathbf{q}}{2}) \psi_{+,\mathbf{G}',l}(\mathbf{k}' + \frac{\mathbf{q}}{2}), \quad (4) \end{aligned}$$

where $\psi_{\tau,l}^{\dagger}$ is the creation operator for electrons in valley $\tau = \pm$ and layer l , A is the sample area, \mathbf{G} and \mathbf{G}' are moiré reciprocal lattice vectors. In this Letter, we use $g = 120 \text{ meV}\cdot\text{nm}^2$ [9] for our calculations. The qualitative results, expressed in dimensionless units, do not depend on the specific choice of g . Using the single-band approximation, the band-projected interaction takes the form

$$\begin{aligned} \mathcal{H}_{\text{int}} = -\frac{g}{A} \sum_{l,\mathbf{k},\mathbf{k}'} u_{\mathbf{k},l}^*(\mathbf{q}) u_{\mathbf{k}',l}(\mathbf{q}) c_+^{\dagger}(\mathbf{k} + \frac{\mathbf{q}}{2}) c_-^{\dagger}(-\mathbf{k} + \frac{\mathbf{q}}{2}) \\ c_-(-\mathbf{k}' + \frac{\mathbf{q}}{2}) c_+(\mathbf{k}' + \frac{\mathbf{q}}{2}), \quad (5) \end{aligned}$$

where $c_{\tau}^{\dagger}(\mathbf{k}) = \sum_{l,\mathbf{G}} z_{\tau\mathbf{G}l}(\mathbf{k}) \psi_{\tau\mathbf{G}l}^{\dagger}(\mathbf{k})$ is the creation operator in band representation, and $u_{\mathbf{k},l}(\mathbf{q}) = \sum_{\mathbf{G}} z_{+,\mathbf{G},l}(\mathbf{k} + \mathbf{q}/2) z_{-,-\mathbf{G},l}(-\mathbf{k} + \mathbf{q}/2)$.

The Bogoliubov-de Gennes Hamiltonian with spinor $\Psi_{\mathbf{k}}^{\dagger} = (c_+^{\dagger}(\mathbf{k} + \mathbf{q}/2) \ c_-(-\mathbf{k} + \mathbf{q}/2))$ is

$$H_{\text{BdG}}(\mathbf{k}) = \begin{pmatrix} \xi_+(\mathbf{k} + \frac{\mathbf{q}}{2}) & \Delta_{\mathbf{q}} \\ \Delta_{\mathbf{q}}^* & -\xi_-(-\mathbf{k} + \frac{\mathbf{q}}{2}) \end{pmatrix}, \quad (6)$$

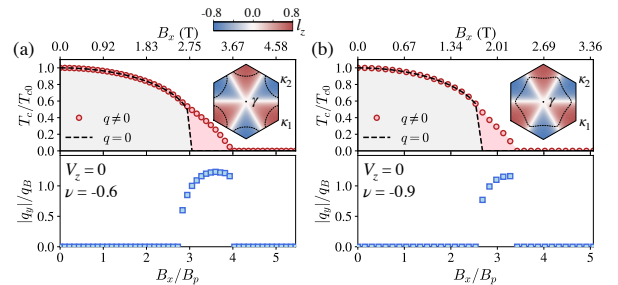


FIG. 2. T_c vs. B_x and the Cooper pair momentum corresponding to the highest T_c of 3.65° tWSe₂ for layer symmetric case $V_z = 0$ at (a) $\nu = -0.6$ and (b) $\nu = -0.9$. Hexagonal insets: layer polarization $l_z(\mathbf{k})$ in the moiré Brillouin zone (MBZ), sharing the same colorbar on the top left. Black dashed contours depict corresponding FSs. The top x -axes show B_x in Tesla for reference, using an attraction strength $g = 120 \text{ meVnm}^2$.

$\xi_\tau = \varepsilon_\tau - \mu$ is the band energy measured from the chemical potential. $\Delta_{\mathbf{q}} = \sum_l u_{\mathbf{k},l}^*(\mathbf{q}) \tilde{\Delta}_{\mathbf{q},l}$ is the superconducting order parameter. We define the layer-resolved superconducting order parameter

$$\tilde{\Delta}_{\mathbf{q},l} = -\frac{g}{A} \sum_{\mathbf{k}} u_{\mathbf{k},l}(\mathbf{q}) \langle c_-(-\mathbf{k} + \frac{\mathbf{q}}{2}) c_+(\mathbf{k} + \frac{\mathbf{q}}{2}) \rangle. \quad (7)$$

The linearized gap equation is

$$\tilde{\Delta}_{\mathbf{q},l} = \sum_{l'} \chi_{ll'}(\mathbf{q}) \tilde{\Delta}_{\mathbf{q},l'}, \quad (8)$$

where $\chi_{ll'}$ is the matrix element of the superconducting pair susceptibility

$$\begin{aligned} \chi_{ll'}(\mathbf{q}) &= \frac{g}{A} \sum_{\mathbf{k}'} u_{\mathbf{k}',l}(\mathbf{q}, \mathbf{B}) u_{\mathbf{k}',l'}^*(\mathbf{q}, \mathbf{B}) \\ &\quad \frac{1 - f(\xi_+(\mathbf{k}' + \frac{\mathbf{q}}{2}, \mathbf{B})) - f(\xi_-(-\mathbf{k}' + \frac{\mathbf{q}}{2}, \mathbf{B}))}{\xi_+(\mathbf{k}' + \frac{\mathbf{q}}{2}, \mathbf{B}) + \xi_-(-\mathbf{k}' + \frac{\mathbf{q}}{2}, \mathbf{B})}, \end{aligned} \quad (9)$$

with Fermi-Dirac distribution $f(\xi) = [e^{\xi/k_B T} + 1]^{-1}$. The superconducting transition temperature $T_c = \max\{T_c(\mathbf{q})\}$ [60], and $T_c(\mathbf{q})$ is the temperature at which the largest eigenvalue of matrix χ reaches one. To streamline numerical calculations, we approximate $\varepsilon(\mathbf{k}, \mathbf{B})$ and $u_{\mathbf{k},l}(\mathbf{q}, \mathbf{B})$ using small-momentum and weak-field expansions [56]:

$$u_{\mathbf{k},l}(\mathbf{q}, \mathbf{B}) \approx \sum_{\mathbf{G}} |z_{+,l,\mathbf{G}}(\mathbf{k})|^2, \quad (10)$$

$$\varepsilon(\mathbf{k}_0 + \mathbf{q}, \mathbf{B}) \approx \varepsilon(\mathbf{k}_0, B = 0) + \mathbf{v}(\mathbf{k}_0) \cdot \mathbf{q} + \mathbf{M}(\mathbf{k}_0) \cdot \mathbf{B},$$

where $\mathbf{v}(\mathbf{k}) = \partial_{\mathbf{k}} \varepsilon|_{B=0}$, $\mathbf{M}(\mathbf{k}) = \partial_{\mathbf{B}} \varepsilon|_{B=0}$, which are provided in the SM [56] for twist angles $2^\circ, 3.65^\circ$ and 6° . We have numerically checked several cases using full calculations without performing expansions.

Layer symmetric case ($V_z = 0$). We first discuss the zero displacement field case, where the system remains layer-unpolarized with $\bar{l}_z = 0$ at any filling. Figure 2 shows T_c as a function of $\mathbf{B} = B_x \hat{x}$ [61] for two different filling factors, $\nu = -0.6, -0.9$, with distinct FSs as shown in the insets of Fig. 2. Despite the differences in the FS geometry at these fillings, the phase diagrams remain qualitatively similar due to the preserved layer symmetry. In particular, phase diagrams in Fig. 2 are reminiscent of that in Zeeman-driven FFLO systems [34–36, 62–64]. At small $B_{||}$, the system remains in a BCS-type ($q = 0$) superconducting phase (gray region in Fig. 2). However, for temperatures below $T/T_{c0} \sim 0.56$ and high fields $B_x/B_p \gtrsim 3$ [65], the system transitions into a finite- q superconducting state (pink region in Fig. 2), where Cooper pairs acquire a finite momentum $q \sim q_B = d/l_B^2$ which is perpendicular to

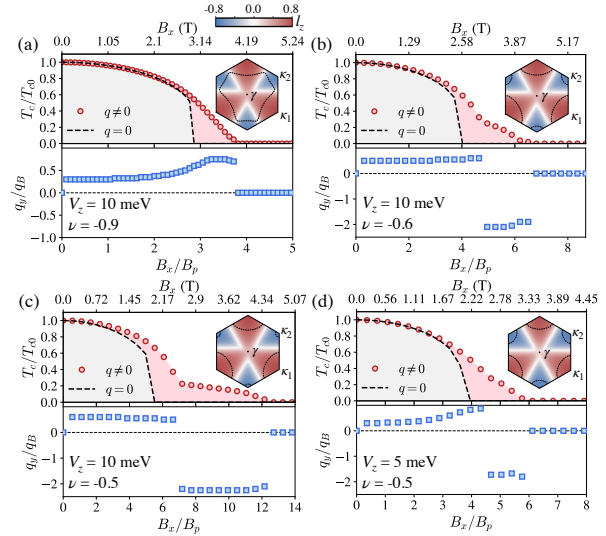


FIG. 3. T_c vs. B_x and the Cooper pair momentum corresponding to the highest T_c of 3.65° tWSe₂ for layer asymmetric cases. V_z and ν are indicated in each sub-figure. An FF phase can be stabilized at any nonzero B_x . The evolution of Cooper pair momentum with B_x depends on the FS geometry.

the applied in-plane field (lower panels of Fig. 2). Here, T_{c0} is the zero-field critical temperature, and $B_p = 1.86T_{c0}$ denotes the Pauli paramagnetic limit. For the layer-unpolarized case, the superconducting order parameters associated with opposite momenta $\Delta_{\pm\mathbf{q}}$ are nearly degenerate [20], so only $|q_y|$ is shown in Fig. 2. As discussed in Ref. [20], it is believed that FF state is more energetically favorable than the Larkin-Ovchinnikov state in tWSe₂.

Layer asymmetric case ($V_z > 0$). A finite displacement field breaks layer symmetry, causing carriers to favor one layer (layer $l = 1$ for $V_z > 0$). Unlike the layer symmetric case [Fig. 2], where the FF phase requires a finite $B_{||}$, finite- q pairing is stabilized at any nonzero $B_{||}$, as shown in Figs. 3-4. Notably, the degeneracy between \mathbf{q} and $-\mathbf{q}$ is lifted, and all finite- q pairing states are FF states.

For a small displacement field, $V_z \lesssim 20$ meV, the Cooper pair momentum evolves with increasing B_x , depending on the FS geometry. When two separate FSs exist at κ_1 and κ_2 , associated with opposite layers [Fig. 3(b-d)], the phase diagram features a transition between two distinct FF phases with different pairing momenta. This phase transition is marked by a discontinuous jump in \mathbf{q} , particularly in its direction. At small B_x , pairing near T_c is dominated by carriers from κ_1 , where larger layer polarization results in a smaller q . As B_x increases, the dominant pairing shifts to κ_2 , which has a larger q . This

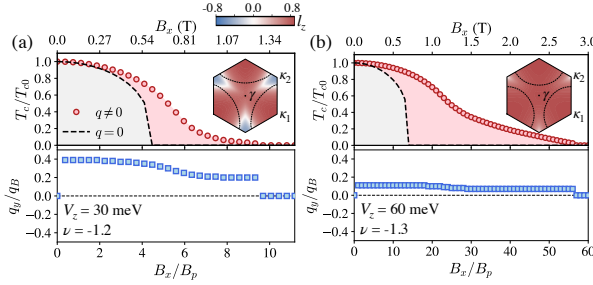


FIG. 4. T_c vs. B_x and the Cooper pair momentum corresponding to the highest T_c in 3.65° tWSe₂ for large displacement fields. These filling factors are chosen to maintain similar FS geometries.

phase transition is more pronounced when the two FSs differ significantly in layer polarization [Fig. 3(b-d)], and its location in (ν, V_z) phase diagram is highlighted as yellow-shaded region in Fig. 1(b). In contrast, when a single FS is present [Fig. 3(a)], the Cooper pair momentum evolves smoothly with B_x within the FF phase, reflecting the gradual change in the dominant layer contribution to pairing.

As layer polarization increases with larger V_z , the FF phase expands over a broader region of the phase diagram, as shown in Fig. 4. At low temperatures, both the critical field for the transition from $q = 0$ to $q \neq 0$ superconducting phase ($B_{c1,\parallel}$, gray to pink) and the transition from $q \neq 0$ superconducting phase to the normal state ($B_{c2,\parallel}$, pink to white) increase with V_z . Remarkably, $B_{c2,\parallel}$ can be several times higher than $B_{c1,\parallel}$, indicating a significantly extended FF phase. However, the increasing layer polarization leads to a reduction in the Cooper pair momentum q , this trend is illustrated in Fig. 4 for $V_z = 30$ to 60 meV.

Discussion. The most interesting prediction in this Letter is the emergence of a phase transition within the FF phase, characterized by a sign-changing jump in \mathbf{q} . This transition occurs when the layer symmetry is broken and two distinct FSs associated with different layers are present [Region III in Fig. 1(b)]. Although T_c does not show discontinuity at this transition, the superconducting diode effect can probe the change of \mathbf{q} by measuring supercurrents in two opposite directions (typically perpendicular to the applied magnetic field) [20, 66–74].

Next, we discuss the dependence on the twist angle θ . For smaller twist angles ($\theta \lesssim 4^\circ$), where the moiré bands are flatter, an in-plane field has relatively stronger orbital effects, distorting the FS more significantly and resulting in a smaller region for FF states. As θ increases, the FF phase extends over a broader region in the (B, T) phase diagram, with the

tricritical point at $V_z = 0$ moving to higher temperatures and smaller B fields, suggesting a smaller in-plane magnetic field to induce FF state. The phase diagrams for different θ can be found in SM [56]. A related situation is filling near the VHS, where the dispersion becomes significantly flat. In such cases, the FF phase is often suppressed [56].

The direction of the applied in-plane magnetic field also plays an important role in shaping the FF phase. The orbital effects of B_x and B_y result in different FS deformations (see Figs. S1-S2 in SM [56]). A clear example occurs when a single Fermi pocket is around the γ point at $V_z = 0$: Under B_x , the FS undergoes distortions that create nearly “nesting” Fermi sheets separated vertically, favoring a finite- q_y pairing; In contrast, the FS reshaping under B_y is very different, making the FF phase less favorable in this case. Further details on the effects of B_y , including the corresponding phase diagrams, are provided in the SM [56]. For $V_z \neq 0$, the dependence on field direction becomes more complex, influenced by detailed features of the FS, layer polarization, and $\mathbf{v}(\mathbf{k})$ and $\mathbf{M}(\mathbf{k})$ distributions. Nevertheless, the general properties of the FF phase we described in Figs. 2-4, including the phase transition within the FF phase, remain valid for $\mathbf{B} = B_y \hat{y}$.

An implicit assumption in this Letter is that the pairing glue is *not* affected by B_\parallel . Meanwhile, several recent studies suggest the possibility of spin-fluctuation mechanism [3, 6] (as inferred by the moiré Hubbard model, e.g., Ref. [75]), in which case B_\parallel may polarize spin and suppress superconductivity concomitantly and $B_{c2,\parallel}$ should be much smaller, possibly below B_p . In addition, the theories based on the moiré lattice model predict the pairing symmetry different than the intervalley intralayer pairing discussed in this work [3]. Despite this, the orbital FFLO states should be generic and independent of pairing symmetry, provided B_\parallel is sufficiently strong. A systematic study incorporating different pairing mechanisms and symmetries is an important future direction, but our predicted FFLO physics in an in-plane field should be robust.

Finally, we comment on the B_\parallel response for 2D superconductivity in graphene-based materials. Graphene multilayers present additional complications due to significant Zeeman effects. An intriguing exception is the recently discovered intervalley spin-polarized superconductivity in electron-doped rhombohedral graphene tetralayers and pentalayers [76], which has motivated a number of theoretical studies [77–89]. In particular, incommensurate finite- \mathbf{q} pairing is expected even without B_\parallel [81, 90, 91]. Experiments have reported in-plane

critical fields far exceeding the Pauli limit, suggesting a rich phase diagram for orbital FF states. The superconducting diode effect [20, 66–74] provides a promising avenue to probe these states [92].

Acknowledgments. We thank Liang Fu, Jay D. Sau, and Puhua Wan for valuable discussions. This work is supported by the Laboratory for Physical Sciences.

-
- [1] Y. Guo, J. Pack, J. Swann, L. Holtzman, M. Cothrine, K. Watanabe, T. Taniguchi, D. G. Mandrus, K. Barmak, J. Hone, A. J. Millis, A. Pa-supathy, and C. R. Dean, *Superconductivity in 5.0° twisted bilayer WSe₂*, *Nature* **637**, 839 (2025).
- [2] Y. Xia, Z. Han, K. Watanabe, T. Taniguchi, J. Shan, and K. F. Mak, *Superconductivity in twisted bilayer WSe₂*, *Nature* **637**, 833 (2025).
- [3] A. Fischer, L. Klebl, V. Crépel, S. Ryee, A. Rubio, L. Xian, T. O. Wehling, A. Georges, D. M. Kennes, and A. J. Millis, *Theory of intervalley-coherent AFM order and topological superconductivity in tWSe₂*, [arXiv:2412.14296](#).
- [4] C. Schrade and L. Fu, *Nematic, chiral and topological superconductivity in transition metal dichalcogenides*, [arXiv:2110.10172](#).
- [5] L. Klebl, A. Fischer, L. Classen, M. M. Scherer, and D. M. Kennes, *Competition of density waves and superconductivity in twisted tungsten diselenide*, *Phys. Rev. Res.* **5**, L012034 (2023).
- [6] A. V. Chubukov and C. M. Varma, *Quantum criticality and superconductivity in twisted transition metal dichalcogenides*, *Phys. Rev. B* **111**, 014507 (2025).
- [7] D. Guerci, D. Kaplan, J. Ingham, J. H. Pixley, and A. J. Millis, *Topological superconductivity from repulsive interactions in twisted WSe₂*, [arXiv:2408.16075](#).
- [8] W. Qin, W.-X. Qiu, and F. Wu, *Kohn-Luttinger Mechanism of Superconductivity in Twisted Bilayer WSe₂: Gate-Tunable Unconventional Pairing Symmetry*, [arXiv:2409.16114](#).
- [9] J. Zhu, Y.-Z. Chou, M. Xie, and S. Das Sarma, *Superconductivity in twisted transition metal dichalcogenide homobilayers*, *Phys. Rev. B* **111**, L060501 (2025).
- [10] T. Chuyi, L. Ming-Rui, Z. Wu, W. Sun, and H. Yao, *Theory of Topological Superconductivity and Anti-ferromagnetic Correlated Insulators in Twisted Bilayer WSe₂*, [arXiv:2409.06779](#).
- [11] S. Kim, J. F. Mendez-Valderrama, X. Wang, and D. Chowdhury, *Theory of correlated insulators and superconductor at $\nu = 1$ in twisted WSe₂*, *Nature Communications* **16**, 1701 (2025).
- [12] A. Wietek, J. Wang, J. Zang, J. Cano, A. Georges, and A. Millis, *Tunable stripe order and weak superconductivity in the Moiré Hubbard model*, *Phys. Rev. Res.* **4**, 043048 (2022).
- [13] M. Christos, P. M. Bonetti, and M. S. Scheurer, *Approximate symmetries, insulators, and superconductivity in continuum-model description of twisted WSe₂*, [arXiv:2407.02393](#).
- [14] F. Xie, L. Chen, S. Sur, Y. Fang, J. Cano, and Q. Si, *Superconductivity in twisted WSe₂ from topology-induced quantum fluctuations*, [arXiv:2408.10185](#).
- [15] D. Le, A. Barinov, E. Preciado, M. Isarraraz, I. Tanabe, T. Komesu, C. Troha, L. Bartels, T. S. Rahman, and P. A. Dowben, *Spin-orbit coupling in the band structure of monolayer WSe₂*, *Journal of Physics: Condensed Matter* **27**, 182201 (2015).
- [16] P. Fulde and R. A. Ferrell, *Superconductivity in a strong spin-exchange field*, *Phys. Rev.* **135**, A550 (1964).
- [17] A. I. Larkin and Y. N. Ovchinnikov, *Nonuniform state of superconductors*, *Sov. Phys. JETP* **20**, 762 (1965).
- [18] P. Wan, O. Zheliuk, N. F. Q. Yuan, X. Peng, L. Zhang, M. Liang, U. Zeitler, S. Wiedmann, N. E. Hussey, T. T. M. Palstra, and J. Ye, *Orbital Fulde-Ferrell-Larkin-Ovchinnikov state in an Ising superconductor*, *Nature* **619**, 46 (2023).
- [19] C.-X. Liu, *Unconventional superconductivity in bilayer transition metal dichalcogenides*, *Phys. Rev. Lett.* **118**, 087001 (2017).
- [20] Y.-M. Xie and K. T. Law, *Orbital Fulde-Ferrell pairing state in moiré Ising superconductors*, *Phys. Rev. Lett.* **131**, 016001 (2023).
- [21] N. F. Q. Yuan, *Orbital Fulde-Ferrell-Larkin-Ovchinnikov state in an Ising superconductor*, *Phys. Rev. Res.* **5**, 043122 (2023).
- [22] N. F. Q. Yuan, *Orbital Fulde-Ferrell State versus Orbital Larkin-Ovchinnikov State*, [arXiv:2502.18075](#).
- [23] D. Zhao, L. Debbeler, M. Kühne, S. Fecher, N. Gross, and J. Smet, *Evidence of finite-momentum pairing in a centrosymmetric bilayer*, *Nature Physics* **19**, 1599 (2023).
- [24] Z. Cao, M. Liao, H. Yan, Y. Zhu, Z. Liguo, K. Watanabe, T. Taniguchi, A. F. Morpurgo, H. Liu, Q.-K. Xue, and D. Zhang, *Spectroscopic evidence for a first-order transition to the orbital Fulde-Ferrell-Larkin-Ovchinnikov state*, [arXiv:2409.00373](#).
- [25] X. Zhao, G. Guo, C. Yan, N. F. Yuan, C. Zhao, H. Guan, C. Lan, Y. Li, X. Liu, and S. Wang, *Orbital Fulde-Ferrell-Larkin-Ovchinnikov state in 2H-NbS₂ flakes*, [arXiv:2411.08980](#).
- [26] C.-w. Cho, T. T. Lortz, K. T. Lo, C. Y. Ng, S. H. Chui, A. R. Allan, M. Abdel-Hafiez, J. Park, B. Cho, K. Park, N. F. Q. Yuan, and R. Lortz, *Evidence for the novel type of orbital Fulde-Ferrell-Larkin-Ovchinnikov state in the bulk limit of 2H-NbSe₂*, [arXiv:2312.03215](#).
- [27] F. Z. Yang, H. D. Zhang, S. Mandal, F. Y. Meng, G. Fabbris, A. Said, P. M. Lozano, A. Rajapita-mahuni, E. Vescovo, C. Nelson, S. Lin, Y. Park, E. M. Clements, T. Z. Ward, H.-N. Lee, H. C. Lei, C. X. Liu, and H. Miao, *Signature of Orbital Driven Finite Momentum Pairing in a 3D Ising Supercon-*

- ductor*, arXiv:2407.10352.
- [28] G.-W. Qiu and Y. Zhou, *Inhomogeneous superconducting states in two weakly linked superconducting ultrathin films*, Phys. Rev. B **105**, L100506 (2022).
- [29] H. Yan, H. Liu, Y. Liu, D. Zhang, and X. C. Xie, *Orbital-FFLO State and Josephson Vortex Lattice Melting in Layered Ising Superconductors*, arXiv:2409.20336.
- [30] U. Nag, J. Schirmer, E. Rossi, C.-X. Liu, and J. K. Jain, *BCS Stripe Phase in Coupled Bilayer Superconductors*, arXiv:2408.00689.
- [31] Y.-T. Hsu, F. Wu, and S. Das Sarma, *Spin-valley locked instabilities in moiré transition metal dichalcogenides with conventional and higher-order van hove singularities*, Phys. Rev. B **104**, 195134 (2021).
- [32] B. S. Chandrasekhar, *A note on the maximum critical field of high-field superconductors*, Appl. Phys. Letters **Vol. 1** (1962).
- [33] A. M. Clogston, *Upper limit for the critical field in hard superconductors*, Phys. Rev. Lett. **9**, 266 (1962).
- [34] D. F. Agterberg, J. S. Davis, S. D. Edkins, E. Fradkin, D. J. Van Harlingen, S. A. Kivelson, P. A. Lee, L. Radzihovsky, J. M. Tranquada, and Y. Wang, *The physics of pair-density waves: Cuprate superconductors and beyond*, Annual Review of Condensed Matter Physics **11**, 231 (2020).
- [35] R. Casalbuoni and G. Nardulli, *Inhomogeneous superconductivity in condensed matter and QCD*, Rev. Mod. Phys. **76**, 263 (2004).
- [36] L. Radzihovsky and D. E. Sheehy, *Imbalanced Feshbach-resonant Fermi gases*, Reports on Progress in Physics **73**, 076501 (2010).
- [37] M. Houzet, A. Buzdin, L. Bulaevskii, and M. Maley, *New Superconducting Phases in Field-Induced Organic Superconductor λ -(BETS)₂FeCl₄*, Phys. Rev. Lett. **88**, 227001 (2002).
- [38] R. A. Klemm, A. Luther, and M. R. Beasley, *Theory of the upper critical field in layered superconductors*, Phys. Rev. B **12**, 877 (1975).
- [39] R. A. Klemm, M. R. Beasley, and A. Luther, *The upper critical field of layered superconductors*, Journal of Low Temperature Physics **16**, 607 (1974).
- [40] V. Barzykin and L. P. Gor'kov, *Inhomogeneous stripe phase revisited for surface superconductivity*, Phys. Rev. Lett. **89**, 227002 (2002).
- [41] Z. Zheng, M. Gong, Y. Zhang, X. Zou, C. Zhang, and G. Guo, *FFLO Superfluids in 2D Spin-Orbit Coupled Fermi Gases*, Scientific Reports **4**, 6535 (2014).
- [42] N. F. Q. Yuan and L. Fu, *Topological metals and finite-momentum superconductors*, Proceedings of the National Academy of Sciences **118**, e2019063118 (2021).
- [43] X. Xi, Z. Wang, W. Zhao, J.-H. Park, K. T. Law, H. Berger, L. Forró, J. Shan, and K. F. Mak, *Ising pairing in superconducting NbSe₂ atomic layers*, Nature Physics **12**, 139 (2016).
- [44] Y. Saito, Y. Nakamura, M. S. Bahramy, Y. Kohama, J. Ye, Y. Kasahara, Y. Nakagawa, M. Onga, M. Tokunaga, T. Nojima, Y. Yanase, and Y. Iwasa, *Superconductivity protected by spin-valley locking in ion-gated MoS₂*, Nature Physics **12**, 144 (2016).
- [45] J. M. Lu, O. Zheliuk, I. Leermakers, N. F. Q. Yuan, U. Zeitler, K. T. Law, and J. T. Ye, *Evidence for two-dimensional Ising superconductivity in gated MoS₂*, Science **350**, 1353 (2015).
- [46] E. Sohn, X. Xi, W.-Y. He, S. Jiang, Z. Wang, K. Kang, J.-H. Park, H. Berger, L. Forró, K. T. Law, J. Shan, and K. F. Mak, *An unusual continuous paramagnetic-limited superconducting phase transition in 2D NbSe₂*, Nature Materials **17**, 504 (2018).
- [47] S. C. de la Barrera, M. R. Sinko, D. P. Gopalan, N. Sivadas, K. L. Seyler, K. Watanabe, T. Taniguchi, A. W. Tsai, X. Xu, D. Xiao, and B. M. Hunt, *Tuning Ising superconductivity with layer and spin-orbit coupling in two-dimensional transition-metal dichalcogenides*, Nature Communications **9**, 1427 (2018).
- [48] X.-W. Zhang, C. Wang, X. Liu, Y. Fan, T. Cao, and D. Xiao, *Polarization-driven band topology evolution in twisted MoTe₂ and WSe₂*, Nature Communications **15**, 4223 (2024).
- [49] F. Wu, T. Lovorn, E. Tutuc, I. Martin, and A. H. MacDonald, *Topological insulators in twisted transition metal dichalcogenide homobilayers*, Phys. Rev. Lett. **122**, 086402 (2019).
- [50] T. Devakul, V. Crépel, Y. Zhang, and L. Fu, *Magic in twisted transition metal dichalcogenide bilayers*, Nature Communications **12**, 6730 (2021).
- [51] H. Yu, M. Chen, and W. Yao, *Giant magnetic field from moiré induced berry phase in homobilayer semiconductor*, National Science Review **7**, 12 (2019).
- [52] D. Zhai and W. Yao, *Theory of tunable flux lattices in the homobilayer moiré of twisted and uniformly strained transition metal dichalcogenides*, Phys. Rev. Mater. **4**, 094002 (2020).
- [53] M. H. Naik and M. Jain, *Ultraflatbands and shear solitons in moiré patterns of twisted bilayer transition metal dichalcogenides*, Phys. Rev. Lett. **121**, 266401 (2018).
- [54] S. Kundu, M. H. Naik, H. R. Krishnamurthy, and M. Jain, *Moiré induced topology and flat bands in twisted bilayer WSe₂: A first-principles study*, Phys. Rev. B **105**, L081108 (2022).
- [55] \mathbf{G}_j are the first-shell moiré reciprocal lattice vectors. We use the continuum model parameters from Ref. [50]: $V = 9$ meV, $\psi = 128^\circ$, $w = 18$ meV, lattice constant $a_0 = 3.317$ Å, and the effective mass $m^* = 0.43m_e$ with m_e being the electron mass.
- [56] See Supplemental Material (SM) at XXX for details of small-momentum and weak-field expansions, $\mathbf{v}(\mathbf{k})$ and $\mathbf{M}(\mathbf{k})$ in the MBZ, Fermi surface deformations in an in-plane field, phase diagrams for other twist angles from 2° - 5° and in $\mathbf{B} = B_y\hat{\mathbf{y}}$.
- [57] F. Wu and S. Das Sarma, *Identification of superconducting pairing symmetry in twisted bilayer graphene using in-plane magnetic field and strain*, Phys. Rev. B **99**, 220507 (2019).

- [58] W. Qin and A. H. MacDonald, *In-plane critical magnetic fields in magic-angle twisted trilayer graphene*, *Phys. Rev. Lett.* **127**, 097001 (2021).
- [59] E. Lake and T. Senthil, *Reentrant superconductivity through a quantum lifshitz transition in twisted trilayer graphene*, *Phys. Rev. B* **104**, 174505 (2021).
- [60] L. Holleis, C. L. Patterson, Y. Zhang, Y. Vituri, H. M. Yoo, H. Zhou, T. Taniguchi, K. Watanabe, E. Berg, S. Nadj-Perge, and A. F. Young, *Nematicity and orbital depairing in superconducting bernal bilayer graphene*, *Nature Physics* (2025), 10.1038/s41567-024-02776-7.
- [61] Due to the C_{3z} rotational symmetry of tWSe₂, the critical in-plane field remains the same for equivalent directions.
- [62] H. Shimahara, *Fulde-Ferrell state in quasi-two-dimensional superconductors*, *Phys. Rev. B* **50**, 12760 (1994).
- [63] L. Radzihovsky, *Fluctuations and phase transitions in larkin-ovchinnikov liquid-crystal states of a population-imbalanced resonant fermi gas*, *Phys. Rev. A* **84**, 023611 (2011).
- [64] K. Yang, *Inhomogeneous superconducting state in quasi-one-dimensional systems*, *Phys. Rev. B* **63**, 140511 (2001).
- [65] The tricritical point temperature of 3.65° tWSe₂, $T_{\text{tric}}/T_{c0} \approx 0.56$, coincidentally matches that of Ref.[35]. However, in tWSe₂, this value depends on the interlayer coupling strength: as the interlayer coupling decreases (or the twist angle increases), the tricritical points shifts to a higher T_{tric}/T_{c0} and lower B/B_p . Unlike in conventional Zeeman-driven FFLO phase diagram, where the transition from $q = 0$ to $q \neq 0$ superconductivity at $T = 0$ occurs at the Pauli limit $B/B_p = 1$, in Ising superconductors, this transition takes place at a higher B/B_p due to orbital effects and Ising SOC.
- [66] F. Ando, Y. Miyasaka, T. Li, J. Ishizuka, T. Arakawa, Y. Shiota, T. Moriyama, Y. Yanase, and T. Ono, *Observation of superconducting diode effect*, *Nature* **584**, 373 (2020).
- [67] L. Bauriedl, C. Bäuml, L. Fuchs, C. Baumgartner, N. Paulik, J. M. Bauer, K.-Q. Lin, J. M. Lupton, T. Taniguchi, K. Watanabe, C. Strunk, and N. Paradiso, *Supercurrent diode effect and magnetochiral anisotropy in few-layer NbSe₂*, *Nature Communications* **13**, 4266 (2022).
- [68] C. Baumgartner, L. Fuchs, A. Costa, S. Reinhardt, S. Gronin, G. C. Gardner, T. Lindemann, M. J. Manfra, P. E. Faria Junior, D. Kochan, J. Fabian, N. Paradiso, and C. Strunk, *Supercurrent rectification and magnetochiral effects in symmetric josephson junctions*, *Nature Nanotechnology* **17**, 39 (2022).
- [69] J.-X. Lin, P. Siriviboon, H. D. Scammell, S. Liu, D. Rhodes, K. Watanabe, T. Taniguchi, J. Hone, M. S. Scheurer, and J. Li, *Zero-field superconducting diode effect in small-twist-angle trilayer graphene*, *Nature Physics* **18**, 1221 (2022).
- [70] B. Pal, A. Chakraborty, P. K. Sivakumar, M. Davydova, A. K. Gopi, A. K. Pandeya, J. A. Krieger, Y. Zhang, M. Date, S. Ju, N. Yuan, N. B. M. Schröter, L. Fu, and S. S. P. Parkin, *Josephson diode effect from cooper pair momentum in a topological semimetal*, *Nature Physics* **18**, 1228 (2022).
- [71] N. F. Q. Yuan and L. Fu, *Supercurrent diode effect and finite-momentum superconductors*, *Proceedings of the National Academy of Sciences* **119**, e2119548119 (2022).
- [72] K. Nakamura, A. Daido, and Y. Yanase, *Orbital effect on the intrinsic superconducting diode effect*, *Phys. Rev. B* **109**, 094501 (2024).
- [73] J. J. He, Y. Tanaka, and N. Nagaosa, *A phenomenological theory of superconductor diodes*, *New Journal of Physics* **24**, 053014 (2022).
- [74] I. Bankier, L. Attias, A. Levchenko, and M. Khodas, *Superconducting diode effect in Ising superconductors*, (2025), arXiv:2503.15115.
- [75] H. Pan, F. Wu, and S. Das Sarma, *Band topology, Hubbard model, Heisenberg model, and Dzyaloshinskii-Moriya interaction in twisted bilayer WSe₂*, *Phys. Rev. Res.* **2**, 033087 (2020).
- [76] T. Han, Z. Lu, Z. Hadjri, L. Shi, Z. Wu, W. Xu, Y. Yao, A. A. Cotten, O. S. Sedeh, H. Weldeyesus, Y. Jixiang, J. Seo, S. Ye, M. Zhou, H. Liu, G. Shi, Z. Hua, K. Watanabe, T. Taniguchi, P. Xiong, D. M. Zumbühl, L. Fu, and L. Ju, *Signatures of Chiral Superconductivity in Rhombohedral Graphene*, (2024), arXiv:2408.15233.
- [77] Y.-Z. Chou, J. Zhu, and S. Das Sarma, *Intravalley spin-polarized superconductivity in rhombohedral tetralayer graphene*, (2024), arXiv:2409.06701.
- [78] C. Yoon, T. Xu, Y. Barlas, and F. Zhang, *Quarter Metal Superconductivity*, (2025), arXiv:2502.17555.
- [79] M. Kim, A. Timmel, L. Ju, and X.-G. Wen, *Topological chiral superconductivity beyond pairing in a fermi liquid*, *Phys. Rev. B* **111**, 014508 (2025).
- [80] Q. Qin and C. Wu, *Chiral finite-momentum superconductivity in the tetralayer graphene*, (2024), arXiv:2412.07145.
- [81] H. Yang and Y.-H. Zhang, *Topological incommensurate Fulde-Ferrell-Larkin-Ovchinnikov superconductor and Bogoliubov Fermi surface in rhombohedral tetralayer graphene*, (2024), arXiv:2411.02503.
- [82] J. Ammar and S.-Z. Lin, *Enhanced Kohn-Luttinger topological superconductivity in bands with nontrivial geometry*, (2024), arXiv:2411.09664.
- [83] J. D. Sau and S. Wang, *Theory of anomalous Hall effect from screened vortex charge in a phase disordered superconductor*, (2024), arXiv:2411.08969.
- [84] Y.-Q. Wang, Z.-Q. Gao, and H. Yang, *Chiral superconductivity from parent Chern band and its non-Abelian generalization*, (2024), arXiv:2410.05384.
- [85] M. Geier, M. Davydova, and L. Fu, *Chiral and topological superconductivity in isospin polarized multilayer graphene*, (2024), arXiv:2409.13829.
- [86] G. Parra-Martinez, A. Jimeno-Pozo, V. T. Phong, H. Sainz-Cruz, D. Kaplan, P. Emanuel, Y. Oreg, P. A. Pantaleon, J. A. Silva-Guillen, and F. Guinea, *Band Renormalization, Quarter Metals, and Chiral Superconductivity in Rhombohedral Tetralayer Graphene*, (2025), arXiv:2502.19474.

- [87] J. May-Mann, T. Helbig, and T. Devakul, *How pairing mechanism dictates topology in valley-polarized superconductors with Berry curvature*, (2025), arXiv:2503.05697.
- [88] F. Gaggioli, D. Guerci, and L. Fu, *Spontaneous vortex-antivortex lattice and Majorana fermions in rhombohedral graphene*, (2025), arXiv:2503.16384.
- [89] Z. Dong and P. A. Lee, *A controllable theory of superconductivity due to strong repulsion in a polarized band*, (2025), arXiv preprint arXiv:2503.11079.
- [90] M. Christos, P. M. Bonetti, and M. S. Scheurer, *Finite-momentum pairing and superlattice superconductivity in valley-imbalanced rhombohedral graphene*, (2025), arXiv:2503.15471.
- [91] Y. Chen and C. Schrade, *Intrinsic superconducting diode effect and nonreciprocal superconductivity in rhombohedral graphene multilayers*, (2025), arXiv:2503.16391.
- [92] D. Sedov and M. S. Scheurer, *Probing superconductivity with tunneling spectroscopy in rhombohedral graphene*, (2025), arXiv:2503.12650.

SUPPLEMENTARY MATERIAL

A. Small-field expansions and Fermi surface deformations

To streamline numerical calculations, we expand $\varepsilon(\mathbf{k}, \mathbf{B})$ and $u_{\mathbf{k},l}(\mathbf{q}, \mathbf{B})$ in Eq. (9) in terms of small momentum and weak field:

$$u_{\mathbf{k},l}(\mathbf{q}, \mathbf{B}) \approx u_{\mathbf{k},l}(q = 0, B = 0) = \sum_{\mathbf{G}} |z_{+,l,\mathbf{G}}(\mathbf{k})|^2, \quad (\text{S1})$$

$$\varepsilon(\mathbf{k}_0 + \mathbf{q}, \mathbf{B}) \approx \varepsilon(\mathbf{k}_0, B = 0) + \mathbf{v}(\mathbf{k}_0) \cdot \mathbf{q} + \mathbf{M}(\mathbf{k}_0) \cdot \mathbf{B}, \quad (\text{S2})$$

$$(\text{S3})$$

where

$$\begin{aligned} \mathbf{v}(\mathbf{k}_0) &= \partial_{\mathbf{k}} \varepsilon|_{\mathbf{k}=\mathbf{k}_0, B=0} = \langle \partial_{\mathbf{k}} H(\mathbf{k}, \mathbf{B}) \rangle|_{\mathbf{k}=\mathbf{k}_0, B=0}, \\ \mathbf{M}(\mathbf{k}_0) &= \partial_{\mathbf{B}} \varepsilon|_{\mathbf{k}=\mathbf{k}_0, B=0} = \langle \partial_{\mathbf{B}} H(\mathbf{k}, \mathbf{B}) \rangle|_{\mathbf{k}=\mathbf{k}_0, B=0}. \end{aligned} \quad (\text{S4})$$

The k -space distributions of $\mathbf{v}(\mathbf{k})$ and $\mathbf{M}(\mathbf{k})$ for twist angles $\theta = 2^\circ, 3.65^\circ$ and 6° are shown in Fig. S1. As θ increases, the effective interlayer coupling weakens, both \mathbf{v} and \mathbf{M} increase (Fig. S1), but their ratio M/v decreases. As a result, the overall q/q_B of the FF phase decreases with increasing θ (Figs. S3-S4). For smaller twist angles, where the moiré bands are flatter, an in-plane field has relatively stronger orbital effects, distorting the Fermi surface more significantly. This trend is reflected by the overall ratio M/v and Fermi surface deformations at different twist angles (Fig. S2). As θ increases, the FF phase extends over a broader region in the (B, T) phase diagram, with the tricritical point at $V_z = 0$ moving to higher temperatures and smaller B fields (Figs. S3-S4). This suggests that a larger twist angle requires a smaller in-plane field to induce the FF state. In addition, the FF phase is often suppressed near VHS, as seen in Fig. S3 (Ib, IIb) and Fig. S4 (Ic), where the in-plane field significantly distorts the Fermi surfaces of opposite valleys into completely different topologies, preventing effective pairing.

At $V_z = 0$, the field-induced in-plane orbital magnetizations satisfy $M_x \propto -v_y \odot l_z$ and $M_y \propto v_x \odot l_z$, where \odot denotes element-wise matrix multiplication. This implies that M_x is symmetric under both $k_x \rightarrow -k_x$ and $k_y \rightarrow -k_y$ in the valley-projected MBZ, whereas M_y is antisymmetric (see Fig. S1). As a result, under B_y , the FF phase is less favorable when the Fermi surface contour crosses both $k_x = 0$ and $k_y = 0$, as illustrated in Fig. S5(b). This can be partially understood by considering the Fermi surface deformations shown in Fig. S2. If every point on a Fermi surface contour has a “nesting” partner requiring a different \mathbf{q} , no single \mathbf{q} is preferred and FF pairing is suppressed. This scenario is more likely under B_y than under B_x , as evident from Figs. S1-S2. In the opposite limit, where every Fermi surface point pairs with a partner at the same \mathbf{q} , the upper critical in-plane field can, in principle, be arbitrarily large (ignoring Zeeman effects). This is the case when the two layers are completely decoupled. The dependence on field direction becomes more complex when the detailed distributions of $\mathbf{v}(\mathbf{k})$ and $\mathbf{M}(\mathbf{k})$, Fermi surface geometry, and layer polarization are considered, especially for $V_z \neq 0$.

B. Twist-angle dependence of phase diagrams under B_x

In Figs. S3-S4, we explore T_c vs. B_x phase diagrams for twist angles ranging from 2° - 5° at $V_z = 0$. As discussed in Sec. , increasing θ reduces the overall q/q_B of the FF phase and expands the FF region in the (B, T) phase diagram. The tricritical point at $V_z = 0$ shifts to higher temperatures and lower B fields with increasing θ (Figs. S3-S4), indicating that a larger twist angle requires a weaker in-plane field to induce the FF state. Near the VHS, the FF phase is suppressed, as seen in Fig. S3 (Ib, IIb) and Fig. S4 (Ic).

C. Phase diagrams under B_y

Figure S5 presents the T_c vs. B_y phase diagrams under the same V_z and ν conditions as those considered for B_x in the main text, allowing a direct comparison. As discussed in Sec. , at $V_z = 0$ and under B_y , when the Fermi surface contour crosses both $k_x = 0$ and $k_y = 0$, the FF phase is less favorable (Fig. S5(b)). A similar suppression occurs in Fig. S5(d) at small V_z . In other cases shown in Fig. S5, the FF phase exhibits general properties consistent with those in Figs. 2-4 in the main text: A phase transition within the FF phase appears when layer symmetry is broken, and two separate Fermi pockets form at the two moiré mini-valleys (Fig. S5(c)); As $|V_z|$ increases, the FF phase region expands (Fig. S5(e,f)). Note that an extra phase transition occurs in Fig. S5(d), though its phase space region is extremely small, which is attributed to the detailed properties of $\mathbf{v}(\mathbf{k})$, $\mathbf{M}(\mathbf{k})$ and Fermi surface.

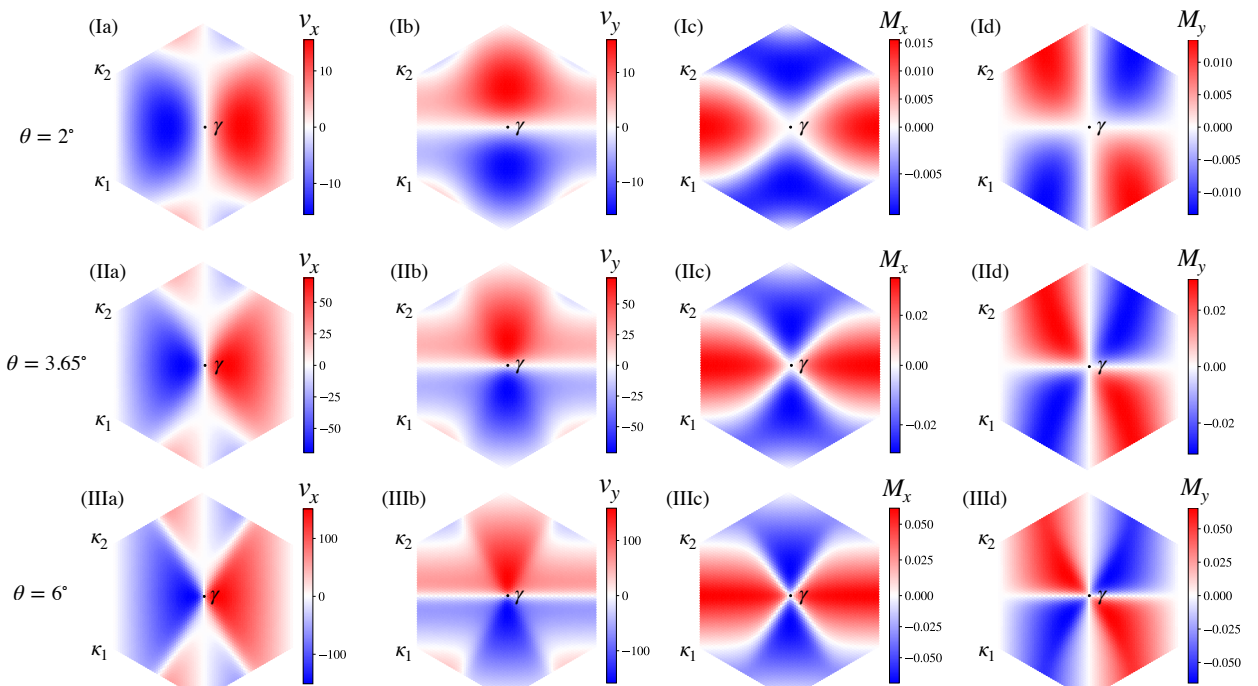


FIG. S1. $\mathbf{v}(\mathbf{k}) \equiv \partial_{\mathbf{k}}\varepsilon|_{B=0}$ and $\mathbf{M}(\mathbf{k}) \equiv \partial_{\mathbf{B}}\varepsilon|_{B=0}$ of valley K for tWSe₂ with $V_z = 0$. (Ia-IId) $\theta = 2^\circ$, (IIa-IIId) 3.65° and (IIIa-IIIId) 6° .

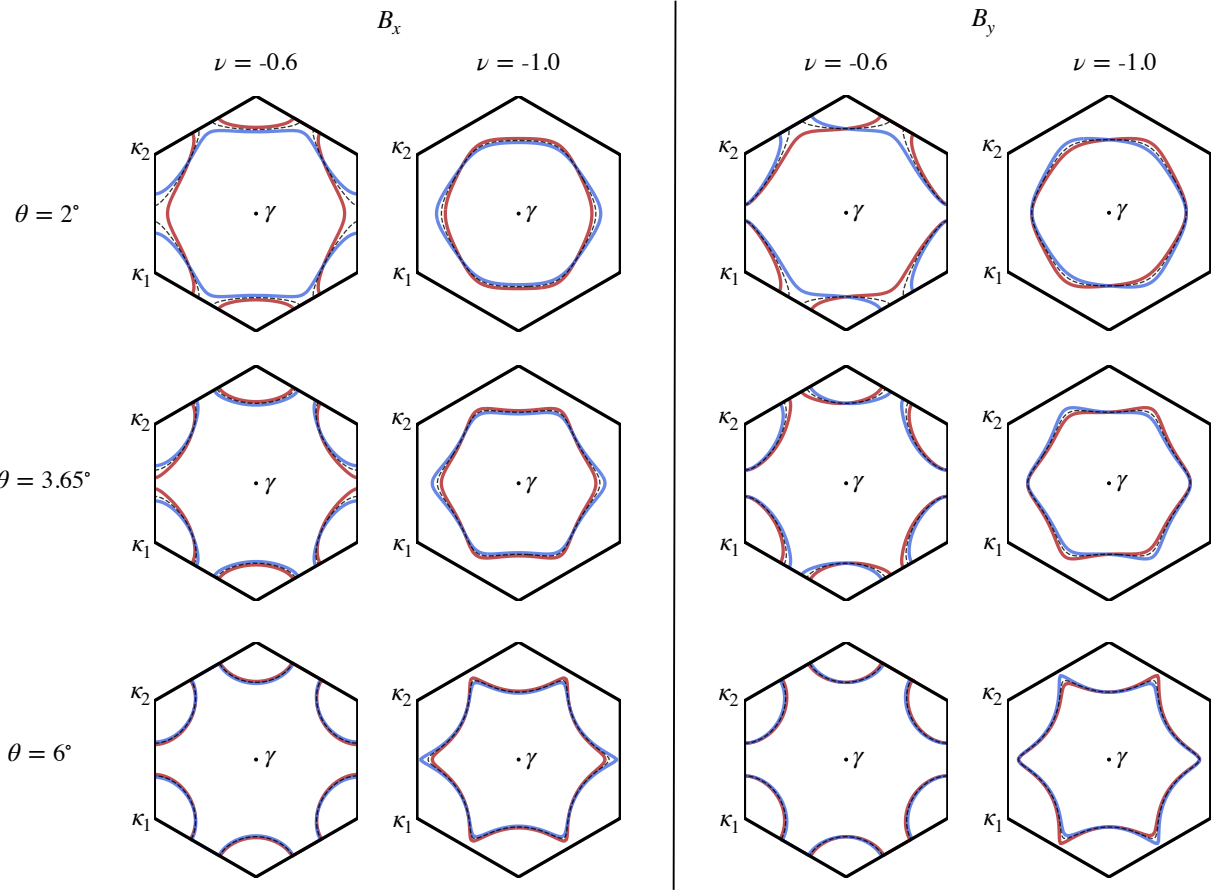


FIG. S2. Fermi surface contours of tWSe₂ at $V_z = 0$ for $\theta = 2^\circ$, 3.65° and 6° . Black dashed lines show the Fermi surface at $B = 0$, which is identical for $\pm K$ valleys. Colored solid lines show Fermi surfaces under an in-plane field: $\mathbf{B} = B_x \hat{x}$ (left) and $\mathbf{B} = B_y \hat{y}$ (right), with red for valley K and blue for valley $-K$. The Fermi surfaces are plotted in the MBZ of valley K , where the blue contours are obtained by applying 2D inversion to those of valley $-K$. To highlight the Fermi surface distortions, large magnetic fields are used: $B = 10$ T for $\theta = 2^\circ$ and $B = 20$ T for $\theta = 3.65^\circ, 6^\circ$.

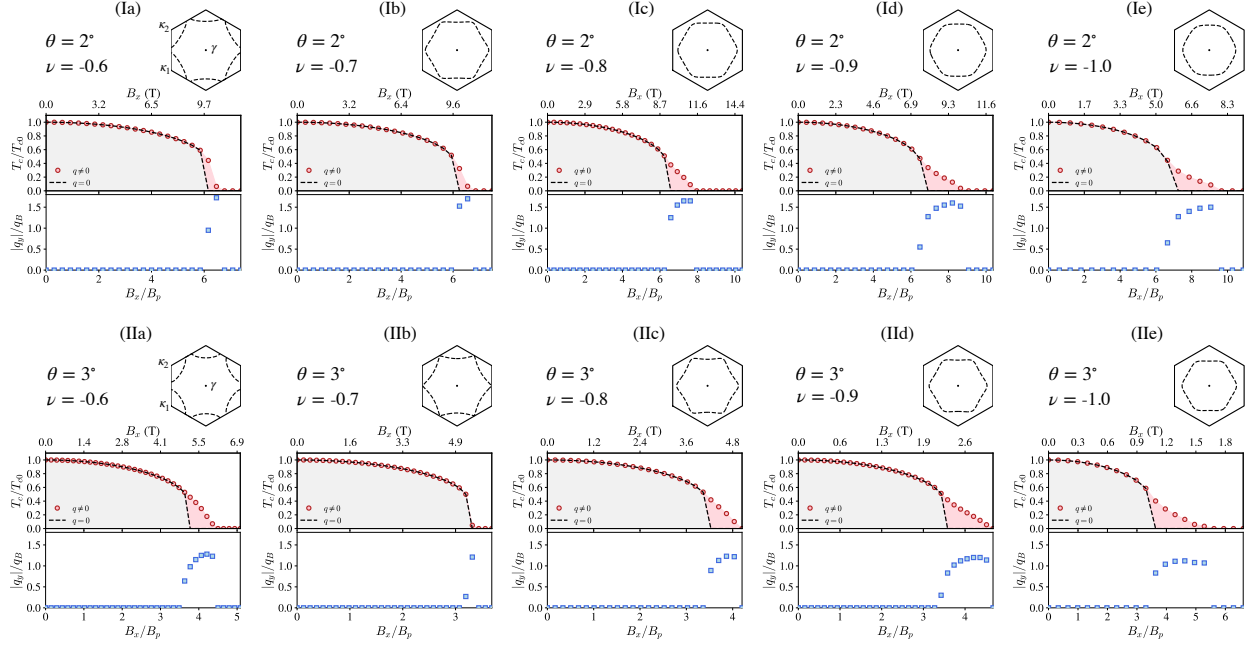


FIG. S3. T_c vs. B_x phase diagram and the Cooper pair momentum corresponding to the highest T_c for tWSe₂ at $V_z = 0$ with twist angles: (Ia-E) $\theta = 2^\circ$ and (IIa-IIe) $\theta = 3^\circ$. The black dashed lines in the hexagonal insets represent Fermi surface contours for the respective filling factors indicated in each subfigure.

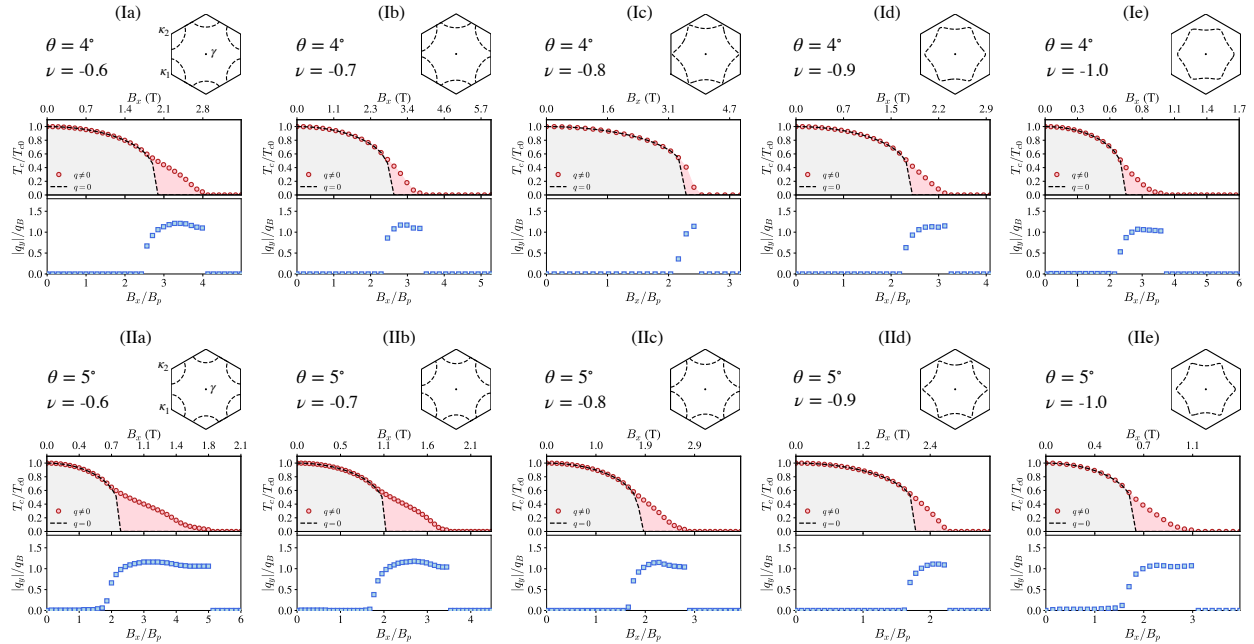


FIG. S4. Same as Fig. S3, but for twist angles: (Ia-E) $\theta = 4^\circ$ and (IIa-IIe) $\theta = 5^\circ$.

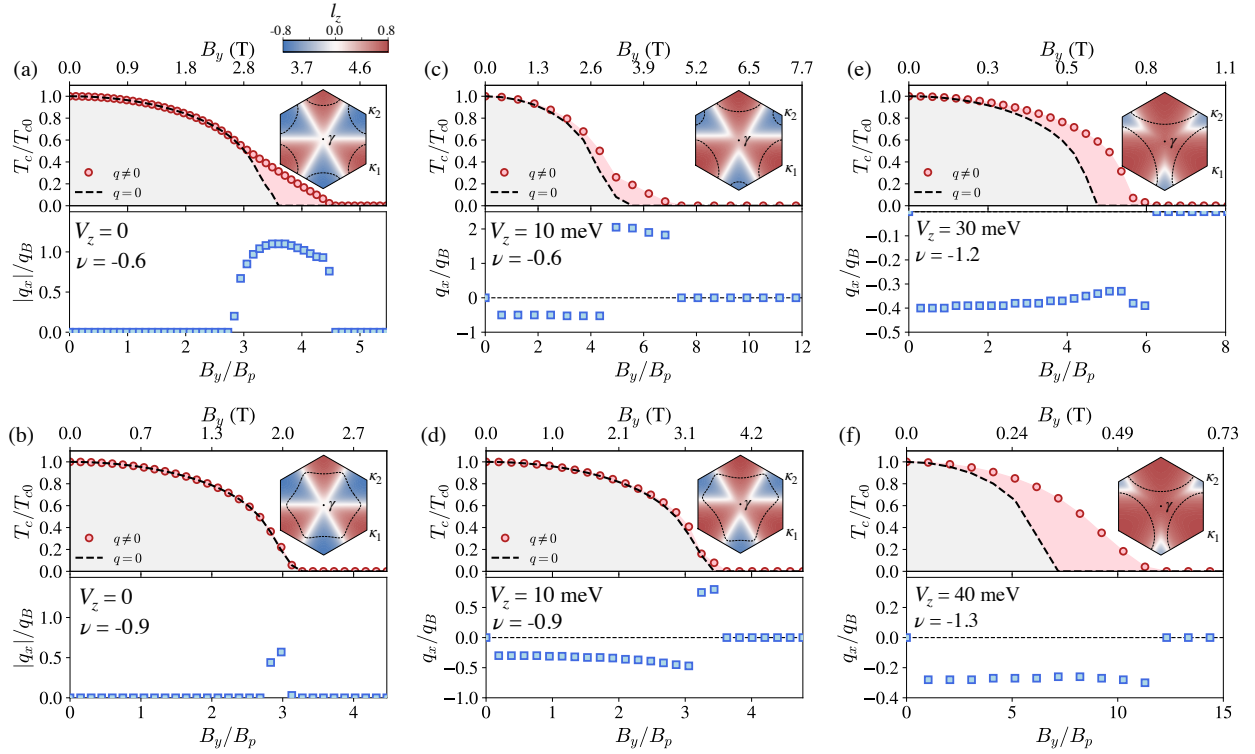


FIG. S5. Phase diagrams under $\mathbf{B} = B_y \hat{\mathbf{y}}$, with the same V_z and filling factors as in Figs. 2,3 of the main text, as indicated in each subfigure.